Earth Planet. Sci. Lett. 679 (2026) 119861

Contents lists available at ScienceDirect

Earth and Planetary Science Letters

journal homepage: www.elsevier.com/locate/epsl

Oxygen vacancy diffusion in davemaoite ($CaSiO_3$ perovskite): Implications for the redox equilibrium and the electrical conductivity of Earth's lower mantle

Maximilian Schulze *, Gerd Steinle-Neumann

Bayerisches Geoinstitut, Universität Bayreuth, 95440, Bayreuth, Germany

ARTICLE INFO

Editor: Dr. Carolina Lithgow-Bertelloni

Keywords:
Perovskite
Oxygen vacancy diffusion
Lower mantle
Redox equilibrium
Ionic conductivity
Arrhenius relation
Machine learning potential molecular dynamics

ABSTRACT

Davemaoite ($CaSiO_3$), a major rock-forming mineral in the Earth's lower mantle, adopts a perovskite structure, which is known for the rapid diffusion of extrinsic oxygen vacancies (OV). Here, we use molecular dynamics simulations in conjunction with a machine learning potential to systematically investigate extrinsic OV diffusion in davemaoite at lower mantle conditions. We determine diffusion coefficients (D_v) for a series of temperatures along isobars of 25, 50, 75, 100 and 125 GPa and find that computed diffusivities closely follow an Arrhenian behavior. The pre-exponential factor is pressure independent with $\log D_v^\circ = -6.53 \pm 0.06$ and the activation enthalpy increases nonlinearly with pressure from 0.87 eV to 1.66 eV. On the basis of the Arrhenian model, we predict that D_v decreases throughout the lower mantle by at least one order of magnitude along geotherms representative of the ambient mantle and subducted lithosphere. We argue that despite the high OV diffusivities, the davemaoite component of subducted oceanic crust does not achieve complete redox equilibration with the surrounding mantle on its way to the core-mantle boundary, and that significant redox exchange is limited to the upper parts of the lower mantle. Finally, we provide arguments that the electrical conductivity of most parts of the lower mantle cannot be explained by ionic conductivity and that its electrical conductivity must therefore be determined by iron-induced polaron hopping.

1. Introduction

Solids with perovskite-type crystal structures are known for their chemical variability and their structurally favored rapid extrinsic oxygen diffusion. For this reason, they play an important role in industrial applications as oxygen-permeable membranes and in solid oxide fuel cells, where oxygen acts as the primary charge carrier for ionic conductivity (Li et al., 2024). These considerations have important implications for deep Earth sciences, given that two of the main mineral phases in the lower mantle (Ishii et al., 2022; Wang et al., 2025a) – bridgmanite ($MgSiO_3$) and davemaoite ($CaSiO_3$) – adopt a perovskite structure. For example, the rate at which oxygen diffuses through davemaoite and bridgmanite in the high-pressure mineral assemblage of subducted oceanic crust (OC) at lower mantle conditions (Ishii et al., 2022) likely determines the degree of redox equilibration reached on its way to the core-mantle boundary (CMB) (Dobson et al., 2008). Moreover, the characterization of oxygen diffusivities in davemaoite and bridgmanite is crucial for interpreting magnetotelluric inversion (Püthe et al., 2015; Verhoeven et al., 2021; Yao et al., 2023) of conductivity profiles of the Earth's interior (Dobson, 2003; Fei et al., 2017; Xu and Mccammon, 2002).

Oxygen diffusion in perovkites is primarily determined by the migration of oxygen vacancies (OV) (Souza, 2015). In the lower mantle, it is expected that vacancies are predominantly extrinsic in nature (Dou et al., 2025; Karki and Khanduja, 2007; Liu et al., 2019), and thus closely coupled to the incorporation of impurities into the respective phase. This formed the basis of several studies on the extrinsic oxygen diffusion (Ammann et al., 2009, 2010b; Karki and Khanduja, 2007) and ionic conductivity of bridgmanite (Dobson, 2003; Xu and Mccammon, 2002). For davemaoite, it has recently been proposed that elevated abundances of extrinsic OVs could potentially trigger a superionic transition at extremely high pressures and temperatures (Wang et al., 2025b). However, a systematic understanding of extrinsic OV diffusion in davemaoite at lower mantle conditions remains lacking.

A major challenge in studying the properties of davemaoite is that it largely eludes experimental investigation, which is due to difficulties in quenching the crystal structure to ambient conditions (Hirose et al., 2005; Irifune and Ringwood, 1993; Miyajima et al., 2025). This

* Corresponding author.
E-mail address: maximilian.schulze@uni-bayreuth.de (M. Schulze).

https://doi.org/10.1016/j.epsl.2026.119861
Received 1 August 2025; Received in revised form 6 December 2025; Accepted 16 January 2026
Available online 27 January 2026
0012-821X/© 2026 The Authors. Published by Elsevier B.V. This is an open access article under the CC BY license (http://creativecommons.org/licenses/by/4.0/).

behavior is particularly problematic for diffusion studies, as they rely on the *ex-situ* characterization of samples recovered from high-pressure experiments (Dobson et al., 2008; Xu et al., 2017, 2011). The investigation of OV diffusion in davemaoite therefore presents a prime goal for the application of molecular dynamics (MD) simulations as a numerical alternative to laboratory experiments. In particular, the recent emergence of machine learning potentials (MLP) (Kocer et al., 2022) offers great potential for studying solid-state diffusion (Li and Scandolo, 2022; Peng and Deng, 2023; Wang et al., 2025b) as they enable MD simulations on timescales far exceeding those of *ab initio* MD simulations. These long time scales provide a promising route to fully converged, statistically significant results for diffusivities in solids, which are otherwise difficult to achieve due to the slow kinetics.

In this study, we developed an MLP to perform an extensive series of MD simulations for the systematic investigation of extrinsic OV diffusion in davemaoite. The diffusion results obtained from these simulations serve as the basis for the parameterization of a model that is capable of predicting OV diffusivity in davemaoite over the entire temperature (T) and pressure (P) range of the lower mantle. We discuss the OV diffusivity in davemaoite in the context of other mantle minerals. Finally, we present the broader implications of our results for understanding redox kinetics of subducted OC and electrical conductivity in the lower mantle.

2. Computational methods

2.1. Construction of the neural network potential and density functional theory calculations

The MLP developed in this study is a Behler-Parinello-type second-generation high-dimensional neural network potential (HDNNP) (Behler and Parrinello, 2007). In this approach, the potential energy, E, of a system consisting of N atoms is described as the sum of the individual atomic energies, E_i,

$$E = \sum_{i=1}^{N} E_i. \tag{1}$$

E_i is calculated based on the local structural geometry within a certain radius R_c, the relationship of which is established by atom-centered symmetry functions (Behler, 2011). We used the n2p2 package for the construction of the HDNNP (Singraber et al., 2019a,b). A total of 92 radial and 429 angular symmetry functions of the forms described by (Behler and Parrinello, 2007) were used with $R_c = 6$ Å. The HDNNP architecture comprises three hidden layers, with 20, 15, and 10 neurons, respectively. The weight parameters were determined using the Kalman filter (Blank and Brown, 1994). The reference data set consisted of potential energies and forces obtained from Kohn-Sham density functional theory (DFT) calculations.

DFT calculations were performed with the Vienna Ab Initio Simulation Package (VASP, version 6.1.2) (Kresse and Furthmüller, 1996) employing the PBE exchange-correlation functional (Perdew et al., 1996) and the projector augmented wave (PAW) method (Kresse and Joubert, 1999). The electronic valence configurations for Ca, Si, and O, explicitly treated by the PAW pseudopotentials, are $3s^2 3p^6 4s^2$, $3s^2 3p^2$, and $2s^2 2p^4$ with core radii of 1.22, 1.01, and 0.80 Å, respectively. The basis set was constructed using an energy cutoff of 850 eV and a $2 \times 2 \times 2$ k-point mesh in the Monkhorst-Pack formalism. These settings result in convergences of energy and pressure within 1 meV atom^{-1} and 0.5 GPa, respectively (Fig. S1 in the supplementary material). The calculations were performed on configurations derived from $3 \times 3 \times 3$ supercells (135 atoms) of the ideal cubic perovskite ($Pm\bar{3}m$) constructed using the Atomsk code (Hirel, 2015), with crystallographic data retrieved from the Materials Project (Jain et al., 2013).

The reference structures were collected in a multi-step process in which MD simulations with preliminary HDNNPs were performed in the isothermal-isobaric ensemble to investigate the configurational space not covered by the underlying training set. New reference structures were selected based on whether they triggered extrapolation warnings or whether the energy difference predicted by two HDNNPs constructed with different random seeds exceeded a threshold of 3 meV atom^{-1} (Tokita and Behler, 2023). The configurational space sampled by the reference structures covered T between 1000 and 5000 K and P between 20 and 150 GPa. The final reference data set comprised a total of 3972 structures: 995 configurations represent the ideal crystal with 135 atoms, 2954 structures contain a CaO Schottky defect and consist of 133 atoms, a small number of 25 structures contain 129 or 132 atoms with one or two SiO_2 Schottky defects. 90 % of the reference data (3582 structures) was used for training, and the remaining 10 % (390 structures) was used for testing in each epoch during the iterative fitting process of the HDNNP.

2.2. Molecular dynamics simulations

MD simulations were performed using the LAMMPS code (version 2 Aug 2023) (Thompson et al., 2022), compiled with an interface to the n2p2 package for energy predictions with the developed HDNNP. The simulations were performed in the canonical ensemble ($N - V - T$), with a constant volume (V) and number of atoms (N), and with a Nosé-Hoover thermostat (damping parameter of 100 fs) controlling T. Periodic boundary conditions in all three dimensions were employed. The time step for the propagation of the atoms was 1 fs, and configurations along the trajectory were saved every 50th time step for post-processing. Production runs each lasted 1 ns, preceded by an equilibration run of 100 ps.

OV diffusion in davemaoite was simulated using systems with 134 atoms, which were constructed by removing an oxygen atom from the $3 \times 3 \times 3$ $Pm\bar{3}m$ supercell. This approach models an infinite dilution of OVs carrying a formal charge of 2+, which follows the example of earlier diffusion studies based on static DFT calculations (Ammann et al., 2009, 2010b; Chen et al., 2023). Finite-size tests with up to 1714 atoms and a single OV showed that the infinite dilution behavior is correctly captured even in relatively small systems of only 134 atoms and that the size of the system does not otherwise influence OV diffusion (Fig. S2). The validity of modeling isolated OVs with the HDNNP trained in this study may not be immediately apparent, as the underlying training set consists exclusively of structures with neutral Schottky pairs, i.e., systems that contain positively charged OVs together with compensating negatively charged cation vacancies. We therefore demonstrate the validity of this approach in Section 3.1.

MD simulations at six T, in steps of 200 K each, were performed along isobars of 25, 50, 75, 100, and 125 GPa. The minimum temperature for each isobar was selected based on whether the number of vacancy hoppings was sufficient to reliably derive diffusion coefficients. The V required for the $N - V - T$ simulations was determined for each $P - T$ point based on simulations of ideal crystals in the $N - P - T$ ensemble. To improve sampling statistics, diffusivities were determined for each condition as the arithmetic mean of ten independent simulations, each conducted with a different initial velocity distribution. The variations of these simulations are communicated in the form of the standard deviation of these ten simulations.

2.3. Analysis of diffusion coefficients

Oxygen diffusion was studied in terms of the mean square displacement,

$$6t D_O = \langle |\boldsymbol{r}(t) - \boldsymbol{r}(0)|^2 \rangle, \tag{2}$$

where $\boldsymbol{r}(t)$ is the position of an oxygen atom at time t. Angular brackets indicate the averages for all oxygen atoms in the system. The time window to record the mean squared displacement was 300 ps. The remaining 700 ps were used to average the result over several intervals. The

analysis was performed using the TRAVIS post-processing code (Brehm and Kirchner, 2011; Brehm et al., 2020). The oxygen tracer diffusion coefficient, D_O, was derived by fitting a linear model to the resulting curve in the time interval between 6 and 150 ps.

Assuming a dilute solution of OVs, the OV diffusion coefficient, D_v, was determined using the relationship

$$D_v = \frac{N_O}{N_v} D_O, \tag{3}$$

where N_O and N_v are the numbers of oxygen atoms and vacancies (Souza, 2015). Focusing on D_v has the advantage that the diffusion coefficients become independent of concentration, which allows for generalization when discussing overall behavior across a wide $P-T$ range. To apply our results beyond the scope of this study, if values for D_O are required, a simple recalculation can be performed using Eq. (3).

3. Results and discussion

3.1. HDNNP

The root mean squared error (RMSE) of the energies is 0.855 meV atom^{-1} for the training set and 0.876 meV atom^{-1} for the test set (Fig. S3). The RMSE of the forces is 0.072 eV Å^{-1} for the training set and 0.073 eV Å^{-1} for the test set. For both, the RMSEs are virtually identical for the training and test sets, which indicates that training was performed on a well-balanced set of configurations, with no signs of significant overfitting. Furthermore, the RMSEs are below the commonly targeted threshold values in the order of 1 meV atom^{-1} and 0.1 eV Å^{-1} (Tokita and Behler, 2023). As a reliability test of the HDNNP, we performed three 1 ns MD simulations of an OV-bearing system (134 atoms) in the microcanonical ensemble at conditions representative of the P–T range covered by the diffusion coefficients under investigation. The energy conservation in these simulations is excellent, with drifts well below 1 meV atom^{-1} ns^{-1} (Fig. S4).

To verify that the HDNNP adequately describes the isolated OV with a formal charge of 2+, we performed a 10 ps MD simulation of an OV-bearing system (134 atoms; no cation vacancy for charge balancing) driven by the HDNNP at 25 GPa and 2000 K. From this simulation, 200 random snapshots were extracted to calculate the forces acting on the atoms using static DFT calculations performed with a deficit of two electrons and a compensating uniform background charge. The HDNNP excellently predicts the forces from these charged DFT calculations, with an RMSE of 0.051 eV Å^{-1} (Fig. S5). This is comparable to the RMSE achieved during training and virtually the same as obtained for a system with a neutral CaO Schottky pair at the same $P-T$ condition as described below. Note that only forces were considered for this benchmark, as the total energies from DFT calculations of charged defects can be affected by spurious electrostatic interactions across the periodic boundaries, and a meaningful comparison would require the application of a correction scheme (Ammann et al., 2010a).

As additional direct benchmarks for the quality of predicted potential energies and forces, as well as for structural and dynamic properties, we performed 15 ps long DFT-MD simulations of a crystal with a CaO Schottky defect at 25 GPa and 2000 K, 75 GPa and 2800 K, and 3600 K and 125 GPa. These simulations used the same strict settings for energy convergence and the k-point mesh as described for the reference calculations. The HDNNP predicts the potential energies and forces of the DFT-MD simulations with RMSEs similar to those obtained for training (Fig. S6). The partial radial distribution functions from the DFT-MD and HDNNP-MD simulations also agree perfectly (Fig. S7), demonstrating that the HDNNP accurately captures the structure of the system. However, comparing diffusivities is less straightforward, as the maximum number of vacancy jumps recorded in the 15 ps DFT-MD simulations is only around ten (Fig. S8), which is far from sufficient for a statistically meaningful evaluation. We therefore compared the oxygen vibrational density of states from the DFT-MD and HDDNP-MD simulations, which we found to be in excellent agreement (Fig. S9). This suggests that the vibrational characteristics can be accurately described by the HDDNP. As vacancy jumps are closely related to the corresponding atomic vibrations, we consider this to be an indicator that diffusion constants can reliably be predicted using the HDNNP.

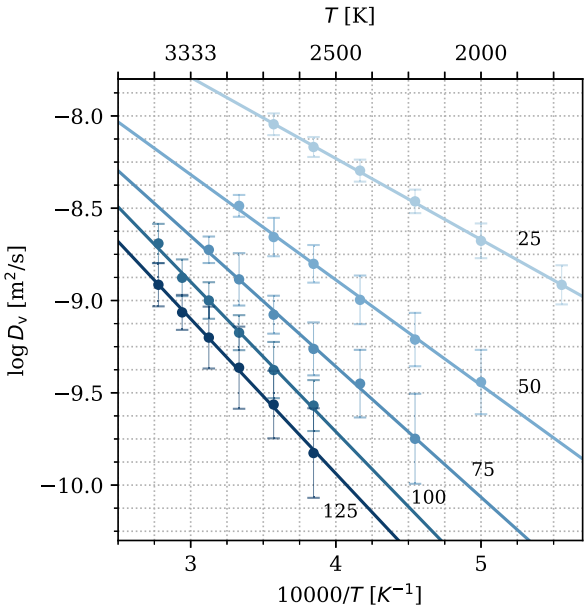

Fig. 1. Oxygen vacancy diffusion coefficients, log D_v, as a function of inverse temperature along five isobars. The solid lines present fits of the Arrhenius-type relation for diffusion coefficients (Eq. (4)). The labels give the respective pressure of each isobar in GPa. Error bars show the standard deviation.

The strongest argument for the reliability of the predicted diffusion coefficients, however, is that they clearly exhibit a physically meaningful behavior by satisfying an Arrhenius relationship, which would be unlikely for inadequately constructed HDNNPs. A detailed discussion follows below.

3.2. Oxygen vacancy diffusion

3.2.1. Arrhenian behavior

D_v spans two orders of magnitude with values ranging from 10^{-10} to 10^{-8} m^2 s^{-1} within the sampled range of conditions (Fig. 1). Along each isobar, the diffusion coefficients increase with T and show Arrhenian behavior, i.e., a linear relationship when plotted as log D_v against T^{-1}. We fitted the logarithmic form of the Arrhenius diffusion coefficient relationship to each isobar,

$$\log D_v = \log D_v^\circ - \frac{\Delta H_a}{\ln(10)\, k_B} \frac{1}{T}, \tag{4}$$

where ΔH_a is the activation enthalpy of diffusion, D_v° is the pre-exponential factor, and k_B is the Boltzmann constant. The fits were performed using the least-squares method as implemented in the SciPy library (Virtanen et al., 2020).

It is worth noting that the validity of the Arrhenius relation for solid-state diffusion at extreme conditions is often only implicitly assumed. In studies using DFT-MD simulations, only a few temperatures are often sampled along a specific isobar due to the high computational cost involved (e.g., Figowy et al., 2024; Mohn et al., 2025). This makes it impossible to truly assess the validity of the linear Arrhenian behavior (Eq. (4)). Furthermore, due to the small sample size, the optimized values for activation enthalpies and pre-exponential factors are often subject to

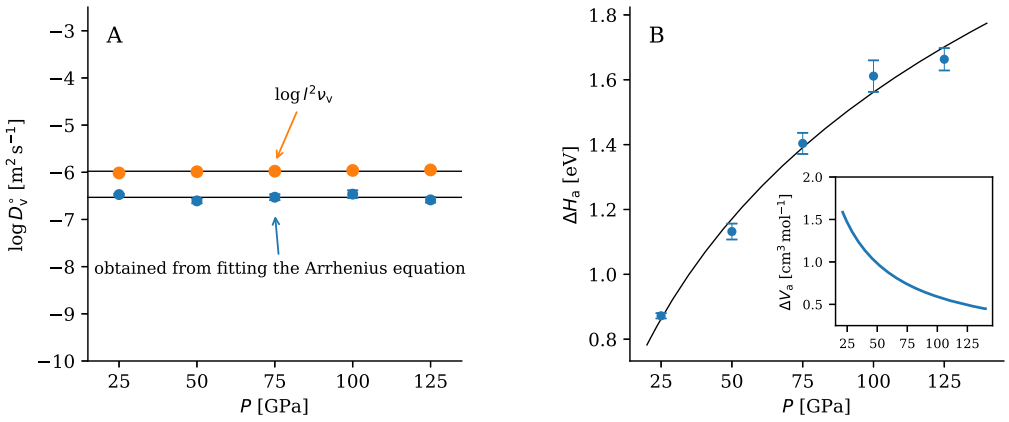

Fig. 2. Arrhenius parameters obtained by fitting Eq. (4) to the diffusion coefficients obtained from the HDNNP-MD simulations (Fig. 1) A) The blue circles show the logarithmic pre-exponential factors, log D_v°. The orange circles show the product of the OV attempt frequency, ν_v, and the square of the OV jump distance, l, which is proportional to D_v° according to the jump rate model of diffusion (Eq. (5)). B) Activation enthalpies, ΔH_a, with the black solid line presenting a fit of Eq. (7). The inset shows the derived activation volume $\Delta V_a = \partial \Delta H_a / \partial P$.

Table 1
Arrhenius parameters log D_v° and ΔH_a (Eq. (4)) for the diffusion coefficients along the isobars from 25 to 125 GPa (Fig. 1). Uncertainties quoted are the standard errors of the least-squares fits. Activation volumes ΔV_a were calculated as the pressure derivative of Eq. (7).

Pressure [GPa]	log (D_v° [m^2 s^{-1}])	ΔH_a [eV]	ΔV_a [cm^3 mol^{-1}]
25	-6.47 ± 0.02	0.87 ± 0.019	1.47
50	-6.61 ± 0.05	1.13 ± 0.025	0.98
75	-6.53 ± 0.06	1.40 ± 0.033	0.74
100	-6.46 ± 0.08	1.61 ± 0.049	0.59
125	-6.59 ± 0.06	1.66 ± 0.034	0.49

considerable uncertainty and can therefore be considered rough estimates at best. In studies based on static DFT calculations (e.g., Ammann et al., 2010b; Chen et al., 2023), ΔH_a and D_v° are determined at zero Kelvin, and the Arrhenius relationship is used to predict the T-dependence of D_v. However, T-independence of ΔH_a and D_v° is an assumption, and changes over the range of hundreds to thousands of Kelvin cannot be ruled out in principle. Therefore, it is generally unclear how large the uncertainties in the D_v values extrapolated from the Arrhenius relation are.

Against this background, we calculated the coefficient of determination, R^2, for each isobar. This allows us to evaluate the quality of the linear fits to our results and, therefore, assess the validity of the Arrhenius behavior. For all isobars, we obtained $R^2 > 0.99$, indicating a high degree of consistency in the linear fits to log D_v. However, it is important to acknowledge that the reliability of this metric may be limited by the number of data points of only six per isobar. With such a small sample size, high R^2 values can sometimes arise even in the presence of nonlinear trends, simply due to insufficient resolution to detect curvature. To address this concern, we visually inspected the residuals for each fit (Fig. S10), which show no systematic deviations that would indicate nonlinearity, further supporting the validity of the Arrhenius relationship. On this basis, we use the Arrhenius relationship as a physically sound basis for parameterizing a model that can predict D_v across the $P - T$ conditions of the lower mantle.

3.2.2. Pre-exponential factor

log D_v°, which is the optimized intercept obtained by fitting Eq. (4), remains constant as a function of P within the scatter, with an average value of log $D_v^\circ = -6.53 \pm 0.06$ (Fig. 2A and Table 1). A constant value for D_v° is advantageous, as it reduces the dimensionality and, thus, potentially also the uncertainties of the parameterized model. However, since the physical reason why D_v° remains constant under compression is not immediately obvious, we further investigated this behavior using an approach that is independent of fitting the Arrhenius relationship. For this purpose, we use the jump rate model to describe diffusivities (Souza, 2015), according to which

$$\log D_v^\circ \propto \log \left[l^2 \nu_v \exp\left(\frac{\Delta S_a}{k_B} \right) \right], \tag{5}$$

where ν_v is the attempt frequency, i.e., the number of attempts a vacancy makes to jump to its neighboring site per time unit. l is the distance between these two sites and ΔS_a is the activation entropy. We determined ν_v following the standard interpretation in diffusion theory, according to which an attempt can be interpreted as a vibration of the diffusing species (Vineyard, 1957). Consequently, we estimated ν_v as the average frequency derived from the corresponding vibrational spectra of the oxygen atoms in an ideal crystal (Klerk et al., 2018). l is determined as the position of the first peak of the O-O radial distribution function. The analysis was performed on trajectories obtained along the isotherm at 2600 K, a T that is covered by all isobars in the simulations performed to investigate OV diffusion (Fig. 1). The results for ν_v and l are shown in Fig. S11. This analysis shows that ν_v increases at a rate that compensates the decrease in l^2 with compression. Consequently, the contribution log $l^2\nu_v$ in Eq. (5) alone can describe log D_v° as a constant, increasing insignificantly over the P range considered, with an average value of approximately -6.0 (Fig. 2A). Negligible P-dependence of log $l^2\nu_v$ has been indicated elsewhere for relatively low P (see e.g., Mehrer, 2007), but, to our knowledge, has not been explicitly demonstrated for extrinsic vacancy diffusion in oxides across the full range of lower mantle conditions. Altogether, this observation indicates that the P-dependence of ΔS_a is also negligible, which is an important insight when describing the P-dependence of diffusion in terms of the activation volume

$$\Delta V_a = \frac{\partial \Delta G_a}{\partial P}, \tag{6}$$

where ΔG_a is the Gibbs free energy of activation (Mehrer, 2007). Since ΔS_a appears insensitive to P, Eq. (6) simplifies to $\Delta V_a = \partial \Delta H_a / \partial P$.

For clarity, we note that log $l^2\nu_v$ as shown in Fig. 2A, does not match log D_v° obtained from the Arrhenius fit in absolute terms, due to the simplifications made. A number of constants (including ΔS_a) are ignored (Souza, 2015), and the underlying simulations were performed at an arbitrary finite temperature.

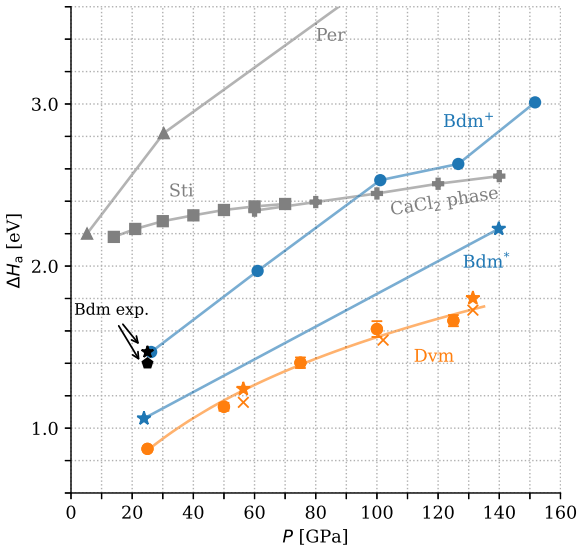

Fig. 3. Activation enthalpies ΔH_a of extrinsic OV diffusion in major mineral phases of the lower mantle. Results for bridgmanite (Bdm), periclase (Per), stishovite (Sti), and the $CaCl_2$-type SiO_2 polymorph were obtained from static density functional theory calculations. Except for the data labeled as Bdm$^+$ (Ammann et al., 2009), all of these calculations were performed in conjunction with the CI-NEB method (Ammann et al., 2010b; Chen et al., 2023). For bridgmanite, average values of ΔH_a for the different jump directions are given in both cases. The results shown for stishovite and the $CaCl_2$-type SiO_2 polymorph are representative of the predominant diffusion paths along the SiO_6 polyhedra, as explained in more detail in Chen et al. (2023). The orange circles show ΔH_a of davemaoite obtained from HDNNP-MD simulations. Orange crosses and stars show ΔH_a of davemaoite obtained from CI-NEB calculations, using $3 \times 3 \times 3$ (135 atoms) and $4 \times 4 \times 4$ (320 atoms) supercells, respectively. The orange solid line represents predictions by Eq. (7). The black star and pentagon show activation enthalpies derived from experimentally determined ionic conductivities of bridgmanite (Dobson, 2003; Xu and Mccammon, 2002).

3.2.3. Activation enthalpies

ΔH_a increases nonlinearly from 0.87 eV at 25 GPa to 1.66 eV at 125 GPa (Fig. 2B and Table 1), well described by the empirical relation

$$\Delta H_a(P) = a \cdot \ln(P + c) + b, \tag{7}$$

with $a = 0.779$ eV, $b = -2.155$ eV, and $c = 25.594$ GPa. From this, we derive ΔV_a values that decrease from 1.47 $cm^3\,mol^{-1}$ at 25 GPa to 0.49 $cm^3\,mol^{-1}$ at 125 GPa (Fig. 2B and Table 1).

Experimental data for the validation of these results is scarce. Fei et al. (2017) report activation values for ionic conduction in davemaoite at 24 GPa. However, they report that the conductivities increase with P, i.e., they exhibit a negative activation volume, which is atypical for ionic conduction. Because this aspect was not discussed further in their work, and detailed chemical characterization of the samples used in these experiments is not available, we refrain from further comparisons with our results.

Previous DFT studies report ΔH_a values of extrinsic OV diffusion in other important solid phases of the lower mantle, including periclase, stishovite, the $CaCl_2$-type SiO_2 polymorph, and bridgmanite (Ammann et al., 2009, 2010b; Chen et al., 2023). These results were obtained from static calculations, with most of them using the climbing image nudged elastic band (CI-NEB) method (Henkelman and Jónsson, 2000; Henkelman et al., 2000). This somewhat complicates direct comparison with our HDNNP-MD simulation results. Therefore, we additionally determined ΔH_a for davemaoite using the CI-NEB method at selected pressures (see Text S1, Fig. S12 and Table S1 in the supplementary material for details), finding very good agreement with Eq. (7) (Fig. 3). On this basis, we consider it reasonable to compare our results with the ΔH_a values reported for the other phases (Ammann et al., 2009, 2010b; Chen et al., 2023) and conclude that davemaoite exhibits the lowest ΔH_a among the major minerals in the lower mantle. Since ΔH_a is usually the main factor determining the magnitude of D_v, it therefore appears likely that davemaoite also has the highest extrinsic OV diffusivity among those minerals.

The literature on bridgmanite provides a possible range of ΔH_a values, which, in all cases, are higher than those for davemaoite (Fig. 3). Ammann et al. (2010b) report ΔH_a values of around 1.1 eV at 24 GPa and 2.2 eV at 140 GPa. This contrasts with an earlier study by the same authors, where they reported a stronger increase from 1.47 eV at 26 GPa to 3.01 eV at 152 GPa, with the corresponding ΔV_a values decreasing from 1.95 $cm^3\,mol^{-1}$ at 25 GPa to 1.49 $cm^3\,mol^{-1}$ at 135 GPa. Overall, these earlier values are in better agreement with experimentally determined enthalpies estimated from ionic conductivities, with Xu and Mccammon (2002) reporting 1.47 eV and Dobson (2003) reporting ~ 1.4 eV at 25 GPa.

Lower ΔH_a values for davemaoite compared to bridgmanite are consistent with the general observation that for perovskites, cubic structures appear to favor faster oxygen diffusion over other crystal symmetries (Li et al., 2024; Robens et al., 2022). Davemaoite has a highly symmetrical crystal structure ($Pm\bar{3}m$), which probably leads to more uniform diffusion paths than in the orthorhombic bridgmanite structure, where the distortion of the SiO_6 octahedra could lead to an increase in migration barriers for certain jump directions, similar to what is observed in other compounds (Li et al., 2024; Yashima, 2008). Furthermore, we speculate that the larger ionic radius of Ca^{2+} compared to Mg^{2+} has two effects that lead to lower migration barriers in davemaoite than in bridgmanite. First, Ca^{2+} causes greater expansion of the lattice free volume, which results in wider diffusion channels for O (Li et al., 2024). Second, Ca^{2+} exhibits weaker electrostatic interactions and thus weaker bonds to the surrounding oxygen atoms than Mg^{2+} (Glasser, 2012).

3.2.4. Model parameterization for predicting oxygen vacancy diffusion

With D_v° and ΔH_a determined, we finally have a closed expression for D_v as a function of P and T with

$$D_v(P,T) = D_v^\circ \exp\left(-\frac{a \cdot \ln(P + c) + b}{k_B T}\right). \tag{8}$$

The values of the four constant parameters D_v°, a, b, and c are summarized in Table S2. The performance of the model is assessed by plotting the predicted D_v values against the values obtained from the HDNNP-MD simulations (Fig. S13). The data points in this plot lie close to a straight line, which is typical for models with high predictive power. As a direct measure of accuracy, we calculated the mean absolute percentage error (MAPE), which yields a global uncertainty of 5 %. Plotting the percentage deviations of the predicted values from the simulation results does not indicate significant overperformance or underperformance at certain pressures (Fig. S11). All simulation values are predicted within a deviation of 10 %. Finally, we verified the extrapolation capability of the model to the conditions at the CMB by performing additional simulations at 135 GPa and T between 2800 and 3600 K. The model accurately predicts the diffusion coefficients obtained from these simulations (Figs. S13 and S14).

4. Geochemical and geophysical implications

In order to discuss the broader implications of our results, we first examined the expected behavior of D_v as a function of P and T in the lower mantle. To this end, we consider two geotherms, representative of the ambient mantle and a subducted slab (Fig. 4A). The geotherms were modeled as adiabats using the Burnman Toolkit (Cottaar et al., 2014; Myhill et al., 2023) with footing temperatures of 1900 K and 1500 K at 25 GPa and using the P-depth relation from the Preliminary reference

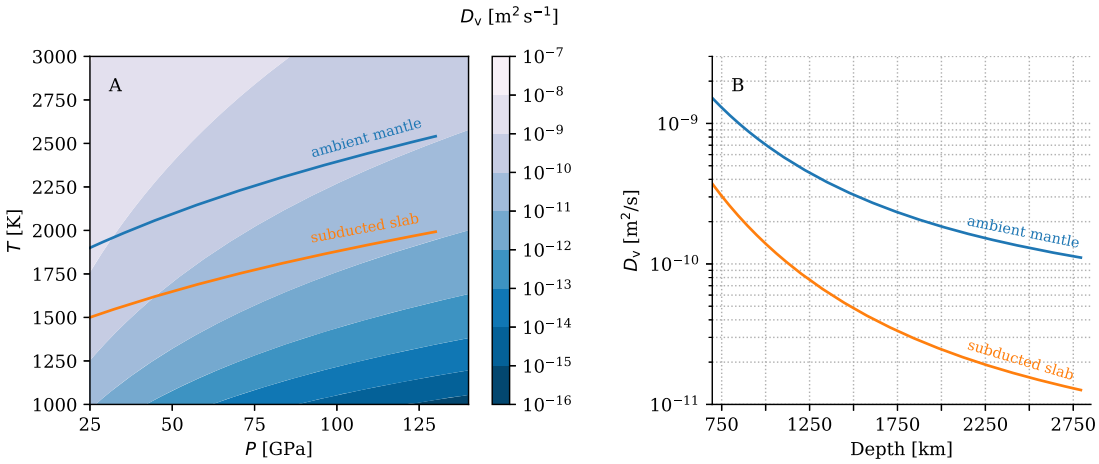

Fig. 4. Behavior of oxygen vacancy diffusivitiy, D_v, in davemaoite as a function of P, T, and depth in the lower mantle. A) The contours show D_v as predicted by Eq. (8). Blue and orange curves show geotherms representative for the ambient lower mantle and subducted slabs, respectively. The adiabats were calculated using the Burnman toolkit (Cottaar et al., 2014; Myhill et al., 2023) with a footing temperature at 25 GP of 1900 K for the ambient mantle, and of 1500 K for the subducted slab. B) D_v as a function of depth along the ambient mantle and subducted slab geotherms.

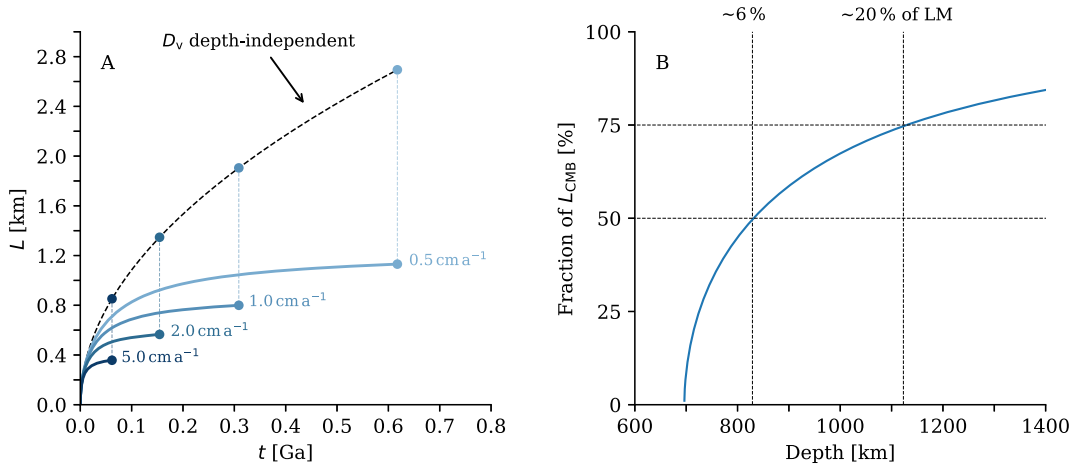

Fig. 5. Characteristic length, L, of OV diffusion in davemaoite used as a proxy for the spatial scales of redox equilibration within a subducted slab. A) The solid curves show L as a function of time as calculated following Eq. (9). Labels indicate different sinking rates of the slab within the lower mantle. For comparison, the dashed curve shows L if D_v were assumed to remain constant at its value at the top of the lower mantle. Round markers show L_{CMB} for the different sinking rates. The corresponding diffusivities are shown in Fig. 4B (orange curve). The slab is assumed to sink with an angle of 45° towards the core-mantle boundary. B) Percentage of the maximum characteristic length, L_{CMB}, as a function of depth. Regardless of the sinking rate, half of L_{CMB} is already reached after penetration of the upper six percent of the lower mantle. 75 % of L_{CMB} is achieved within the upper ~20 % of the lower mantle.

Earth model (Dziewonski and Anderson, 1981). For the sake of simplicity in calculating the adiabats, we assumed thermodynamic parameters of bridgmanite (Stixrude and Lithgow-Bertelloni, 2011).

D_v decreases with P and increases with T (Eq. (8)), which are competing influences on the D_v profiles along the lower mantle geotherms, with the P effect dominating. For the hotter ambient geotherm, D_v decreases by approximately one order of magnitude, from 10^{-9} m^2 s^{-1} at the top to 10^{-10} m^2 s^{-1} at the bottom (Fig. 4B). Diffusion coefficients along the slab geotherm demonstrate a comparably strong decrease, with values approximately one order of magnitude lower.

The decrease in D_v throughout the lower mantle has important implications for the redox kinetics of subducted OC and the role of ionic conduction in the lower mantle.

4.1. Redox kinetics of subducted oceanic crust in the lower mantle

The OC component of subducted slabs with an average thickness of approximately 7 km (White et al., 1992) is considered relatively oxidized compared to the ambient mantle (Evans, 2012), resulting in local redox heterogeneities when transported into the lower mantle. The degree to which the redox contrast at the slab interface can be balanced may largely depend on how quickly OVs diffuse through the individual phases (Dobson et al., 2008). In this context, it is particularly important to understand the behavior of OV diffusion in davemaoite, given its abundance of ~20 vol.% in subducted OC (Ishii et al., 2022; Ono et al., 2001) and its ability to incorporate redox-sensitive elements such as uranium and chromium in considerable amounts (e.g., Britvin et al., 2022; Gréaux et al., 2009). The valence state of these elements could significantly influence their geochemical behavior and the physical properties of the host phase. Therefore, insight into the degree of redox equilibration at the mantle-slab interface can help to understand whether significant changes in such properties are expected when the slab crosses the lower mantle. We note that the following estimates are based exclusively on diffusion in the extrinsic regime and therefore neglect any enthalpy contribution from OV formation, the determination of which would go beyond the scope of this study. The diffusion lengths reported

in the following should thus be considered as upper limits, which will, however, not influence our final conclusions.

As the slab sinks through the lower mantle to the CMB, the maximum redox equilibration length scales, L_{CMB}, that can be achieved via OV diffusion in davemaoite are

$$L_{CMB}^2 \sim \int_0^{t_{CMB}} D_v \, dt, \tag{9}$$

where t_{CMB} is the time at which the slab reaches the CMB, and time integration begins at the top of the lower mantle (25 GPa or 696 km km depth). The slab is assumed to penetrate the lower mantle at an angle of 45 degrees, and the sinking rate is varied over one magnitude from 0.5 cm a^{-1} to 5.0 cm a^{-1}, which results in residence times of the subducted OC in the lower mantle from 62 to 617 Ma (Fig. 5A).

The maximum OV diffusion length reached when the slab arrives at the CMB, L_{CMB}, is highest for the lowest sinking rate of the slab: For 0.5 cm a^{-1}, a distance of about 1.1 km is reached, while for 5 cm a^{-1}, L_{CMB} would be only around 400 m (Fig. 5A, solid lines). In addition to the residence time, this behavior is due to the strong negative dependence of D_v on depth, since a fast sinking rate drives the slab earlier into the low OV diffusivity regime (Fig. 4). The strong negative impact of depth dependence is clearly visible when we monitor the length scales that would be attained if we assumed a constant D_v, in which case L_{CMB} would be overestimated by a factor of 2 to 3 in all cases (Fig. 5A, dashed line). For generally expected sinking rates of $1-2$ cm a^{-1} (Domeier et al., 2016), L_{CMB} is smaller than 1 km. This is significantly smaller than the thickness of the crustal component in the subducting slab, indicating that the bulk of its davemaoite portion cannot be brought into redox equilibrium with the ambient mantle.

The rate at which L increases as a function of time gradually decreases. Consequently, redox equilibration at the slab interface is predicted to be most pronounced in the upper parts of the lower mantle. This becomes more evident when normalizing L to its maximum value, L_{CMB}, which can be used to track the proportional development of L with depth: 50 % of L_{CMB} are already reached at a depth of 830 km, which corresponds to the first 6 % of the lower mantle; 75 % of L_{CMB} are reached at approximately 1120 km, corresponding to the upper 20 % of the lower mantle (Fig. 5B). This observation is important in light of the potential redox gradient of the lower mantle, with its upper portion being relatively oxidized compared to the lower portion (Gu et al., 2016). If this is the case, this could lead to redox differences between the subducted OC and the surrounding mantle, which are lowest in regions with high OV diffusivity and could thus further reduce the already small spatial scales for redox equilibrium across the slab surface.

4.2. Electrical conductivity in the lower mantle

The question of the prevailing electrical transport mechanism in the lower mantle is key to interpreting electrical conductivity profiles from magnetotelluric measurements. The major mechanisms involved are ionic conduction, which is influenced by the defect chemistry of a mineral (Dobson, 2003; Xu and Mccammon, 2002), and small polaron hopping, which is sensitive to the Fe^{2+}-Fe^{3+} ratio (Sinmyo et al., 2014; Yoshino et al., 2016). Early experimental studies revealed high activation enthalpies for ionic conduction compared to small polaron hopping (Dobson, 2003; Xu and Mccammon, 2002), which means that the former mechanism exhibits a stronger increase in conductivity as a function of T. Based on this, it was argued that the effect of increasing temperature with depth might be stronger than that of increasing pressure, leading to the assumption that the electrical conductivity of the deep lower mantle is predominantly ionic in nature (Xu and Mccammon, 2002). However, this idea was questioned on the basis that the P-induced increase in ΔH_a of bridgmanite would probably be significant enough to result in a decrease in ionic conductivity with depth (Yoshino et al., 2016). To date, this has not been investigated in detail.

Here, we address this problem by drawing on the observation that davemaoite is likely the mantle phase with the highest OV diffusivity. This allows us to explore whether ionic conductivity could, in principle, explain the electrical conductivity of the lower mantle in an upper limit scenario. To this end, we use the Nernst-Einstein equation to establish a relationship between ionic conductivity σ_{ion} and D_v,

$$\sigma_{ion} = \frac{z^2 C_v D_v}{k_B T R_H} = \frac{z^2 C_v D_v^\circ}{k_B T R_H} \exp\left(\frac{-\Delta H_a}{k_B T}\right), \tag{10}$$

where z is the charge of oxygen, R_H is the Haven ratio, and C_v is the number of OVs per volume unit. The calculation of σ_{ion} is associated with significant uncertainty, as C_v and R_H are unknown. However, the expected variations in the latter are generally smaller. For simplicity, we therefore assume that $R_H = 1$ and examine how σ_{ion} changes as a function of depth for a wide range of C_v. To estimate the order of magnitude for expected OV concentrations in davemaoite, we consider OV formation by substituting Ca for a monovalent impurity M according to

$$Ca_{Ca}^x + O_O^x \leftrightarrow 2M_{Ca}' + V_O^{\bullet\bullet}.$$

The most important monovalent impurities in davemaoite are K^+ and Na^+, which, according to earlier experiments, account for less than 1 mol % in a pyrolitic mantle and subducted OC (Ishii et al., 2018, 2022; Sun et al., 2024). Using 1 mol % as a guideline and using densities between 4 and 5.5 g cm^{-3}, this results in C_v values in the order of 10^{20} cm^{-3}. Taking into account the uncertainties associated with this estimate, we consider a range of potential OV concentrations between 10^{19} cm^{-3} and 10^{21} cm^{-3} to calculate σ_{ion} following Eq. (10).

For C_v between $10^{20} - 10^{21}$ cm^{-3}, σ_{ion} of davemaoite reaches values that are comparable to the electrical conductivity of the uppermost lower mantle (Fig. 6A). However, σ_{ion} decreases sharply with depth, leading to a significant deviation from magnetotelluric conductivity profiles at a depth of approximately 1250 km for the highest OV concentrations. Since davemaoite is expected to be the mantle phase with the highest OV diffusivity and thus probably also the highest σ_{ion}, we can use these results as an upper limit to conclude that ionic conductivity is probably not a significant mechanism in most parts of the lower mantle.

To further support this conclusion, we consider the problem from a different perspective and discuss the relative behavior of the electrical conductivity in the mantle as a function of depth rather than absolute values. To this end, we use the observation that the electrical conductivity remains approximately constant starting at a depth of around 1000 km (Fig. 6A), and investigate how $\Delta H_a/(k_B T)$, i.e., the exponent in the Arrhenius-type relation of diffusion (Eq. (10)), would have to change as a function of depth in order to reproduce such a behavior:

$$\frac{\Delta H_{a,thresh}}{k_B T} = \ln\left(\frac{1}{\beta T}\right) - \ln(\alpha). \tag{11}$$

$\Delta H_{a,thresh}$ is the activation enthalpy under conditions of constant conductivity, β is a factor ≤ 1 that accounts for the volume reduction upon compression with depth, and α is a material-specific constant (see Text S2 in the supplementary material for derivation). Note that while α influences the absolute value of $\Delta H_{a,thresh}/(k_B T)$, its variation with depth is solely controlled by T and β. To estimate the effect of compression, we consider two cases: (i) $\beta = 1$, i.e., constant volume, and (ii) β decreasing linearly from 1 to 0.75 from the top to the bottom of the lower mantle, which corresponds to a volume reduction of 25 %. As will be demonstrated, the effect of β is only minor for the purposes of the following discussion, and thus the rate at which $\Delta H_{a,thresh}/(k_B T)$ changes with depth can be considered system-independent. Therefore, Eq. (11) is universally valid for studying changes in $\Delta H_{a,thresh}/(k_B T)$, provided that R_H, N_v and D_v° remain constant.

According to Eq. (11), $\Delta H_a/(k_B T)$ would have to decrease by a few percent as a function of depth or, depending on compressibility, remain approximately constant in order to reproduce a constant conductivity

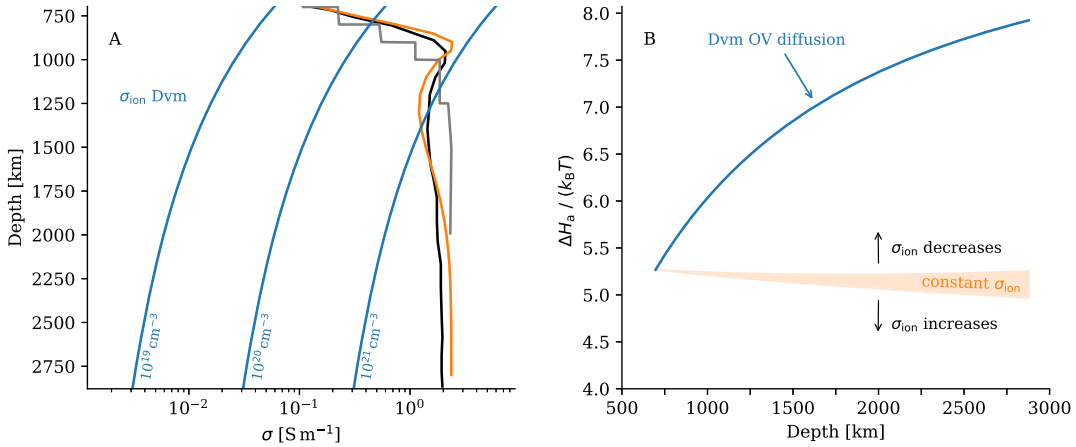

Fig. 6. Ionic conductivity, σ_{ion}, of davemaoite compared to the electrical conductivity of the ambient lower mantle. A) σ_{ion} of davemaoite as calculated after Eq. (10) for different OV concentrations, C_v (blue solid lines, labels indicate C_v). For simplicity, we assumed a Haven ratio, R_H, of one. Black, gray, and orange curves show a representative selection of electrical conductivity profiles of the Earth's lower mantle obtained from magnetotelluric inversion (Püthe et al., 2015; Verhoeven et al., 2021; Yao et al., 2023). B) The orange shaded area shows how $\Delta H_a/(k_B T)$, i.e., the exponent in the Arrhenius-type relation of diffusion, would have to develop in order to yield a constant σ_{ion} with depth. Variations in these values arise from the parameter β in Eq. (11), which accounts for the volume reduction with increasing depth. The lower limit corresponds to a constant volume, and the upper limit to a linear decrease in β from 1 to 0.75, corresponding to a 25 % reduction in volume. The blue curve shows $\Delta H_a/(k_B T)$ for extrinsic OV diffusion in davemaoite.

profile (Fig. 6B). In order for σ_{ion} to increase with depth, $\Delta H_a/(k_B T)$ would have to fall below this threshold. For comparison: $\Delta H_a/(k_B T)$ of davemaoite shows a clear opposite trend and increases by about 50 %. Since davemaoite probably has smaller, at most similar activation volumes as bridgmanite (Fig. 3), we can use this observation as a lower limit to argue that ionic conduction is unlikely to be responsible for the pattern of nearly constant electrical conductivity with depth.

We therefore conclude that the electrical conductivity for much of the lower mantle cannot be explained by ionic conduction, neither in absolute terms nor by its evolution with depth. In agreement with Yoshino et al. (2016), this suggests that ionic conductivity probably plays only a minor role in the deeper ambient lower mantle, and that its electrical conductivity must be governed by iron-induced polaron conduction. For the sake of completeness, we note that this conclusion applies to anhydrous conditions and does not take into account proton-mediated ionic conduction, which was previously proposed as an explanation for the electrical conductivity of at least the upper parts of the lower mantle (Peng and Deng, 2023).

5. Conclusions, caveats, and future studies

Here, we have investigated extrinsic OV diffusion in davemaoite over the $P-T$ range of the lower mantle using MD simulations in conjunction with a MLP. This approach enabled us to show that OV diffusion in davemaoite satisfies the Arrhenius relation, a behavior that has only implicitly been assumed in most diffusion studies. A key aspect in this consideration was the observation that D_v° can be treated as a constant over a wide P range. We emphasize that the high accuracy required to obtain these results is unlikely to be achievable with the limitations of common DFT-MD simulations. We therefore believe that this study is a prime example of how MD simulations assisted by MLPs provide new opportunities to expand our fundamental understanding of the transport properties of solid phases in the deep Earth and other planetary bodies.

The observation that davemaoite is likely the mantle phase with the fastest OV diffusivity enabled us to place new constraints on the redox kinetics of subducted oceanic crust and the electrical structure of the lower mantle. Despite its exceptionally high OV diffusivity, we argue that the davemaoite component in subducted OC is unable to achieve complete redox equilibrium with the ambient mantle on its way to the CMB. With davemaoite likely an upper limit on oxygen diffusion for lower mantle minerals, this conclusion is expected to hold for the entire OC subducted into the lower mantle. Using similar arguments, we provide evidence that ionic conduction is probably not a significant mechanism of electrical conduction in most parts of the lower mantle.

Finally, we acknowledge a number of caveats that were not previously discussed. Our diffusion coefficients are based on the assumption that OVs are present in the dilute limit, i.e., OVs do not interact with each other. Further, we did not explicitly consider the potential effect of vacancy-forming impurities. Both OV-OV and OV-impurity interactions could, in principle, lead to a reduction in the diffusivities (Poirier, 2000; Schie et al., 2012), which is why our results should be considered as upper limits. However, even if these effects operate, the geochemical and geophysical implications discussed above would not be affected. One final aspect that goes beyond the scope of this study is grain boundaries, for which both positive and negative effects on diffusion in perovskite-type solids have been described (Bonkowski et al., 2024). Thus, gaining insights into grain boundary diffusion could provide a new perspective on the timescales of oxygen transport in the lower mantle, making it an interesting subject for future research.

CRediT authorship contribution statement

Maximilian Schulze: Writing – original draft, Visualization, Validation, Resources, Methodology, Investigation, Formal analysis, Data curation, Conceptualization; **Gerd Steinle-Neumann:** Writing – review & editing, Supervision, Resources, Project administration, Methodology, Investigation, Funding acquisition, Conceptualization.

Data availability

Data related to this work can be found in the Open Science Framework under (https://doi.org/10.17605/OSF.IO/M59BP).

Declaration of competing interest

Maximilian Schulze reports financial support was provided by Deutsche Forschungsgemeinschaft (DFG, German Research Foundation). If there are other authors, they declare that they have no known competing financial interests or personal relationships that could have appeared to influence the work reported in this paper.

During the preparation of this work, the authors used DeepL & DeepL Write for language refinement. After using these tools/services, the authors reviewed and edited the content as needed and take full responsibility for the content of the publication.

Acknowledgements

This work is supported by the priority program 2404 DeepDyn of the German Science Foundation (DFG) with grant number 521548786. The authors gratefully acknowledge the Gauss Centre for Supercomputing e.V. https://www.gauss-centre.eu for funding this project by providing computing time on the GCS Supercomputer SuperMUC-NG at Leibniz Supercomputing Centre https://www.lrz.de. We thank Jie Deng and an anonymous reviewer for their constructive comments, which helped improve the manuscript.

Supplementary material

Supplementary material associated with this article can be found, in the online version, at 10.1016/j.epsl.2026.119861

References

Ammann, M.W., Brodholt, J.P., Dobson, D.P., 2009. DFT study of migration enthalpies in $MgSiO_3$ perovskite. Phys. Chem. Miner. 36, 151–158. https://doi.org/10.1007/s00269-008-0265-z

Ammann, M.W., Brodholt, J.P., Dobson, D.P., 2010a. Simulating diffusion. Rev. Mineral. Geochem. 71, 201–224. https://doi.org/10.2138/rmg.2010.71.10

Ammann, M.W., Brodholt, J.P., Wookey, J., Dobson, D.P., 2010b. First-principles constraints on diffusion in lower-mantle minerals and a weak D″ layer. Nature 465, 462–465. https://doi.org/10.1038/nature09052

Behler, J., 2011. Atom-centered symmetry functions for constructing high-dimensional neural network potentials. J. Chem. Phys. 134, 74106. https://doi.org/10.1063/1.3553717

Behler, J., Parrinello, M., 2007. Generalized neural-network representation of high-dimensional potential-energy surfaces. Phys. Rev. Lett. 98, 146401. https://doi.org/10.1103/PhysRevLett.98.146401

Blank, T.B., Brown, S.D., 1994. Adaptive, global, extended Kalman filters for training feedforward neural networks. J. Chemom. 8, 391–407. https://doi.org/10.1002/cem.1180080605

Bonkowski, A., Kilner, J.A., Souza, R.A.D., 2024. Oxygen grain-boundary diffusion in $(La,Sr)FeO_{3-\delta}$ perovskite-oxides probed by molecular-dynamics simulations. RSC Appl. Interf. 1, 699–710. https://doi.org/10.1039/D3LF00263B

Brehm, M., Kirchner, B., 2011. Travis - a free analyzer and visualizer for Monte Carlo and molecular dynamics trajectories. J. Chem. Inf. Model. 51, 2007–2023. https://doi.org/10.1021/ci200217w

Brehm, M., Thomas, M., Gehrke, S., Kirchner, B., 2020. Travis-a free analyzer for trajectories from molecular simulation. J. Chem. Phys. 152, 164105. https://doi.org/10.1063/5.0005078

Britvin, S.N., Vlasenko, N.S., Aslandukov, A., Aslandukova, A., Dubrovinsky, L., Gorelova, L.A., Krzhizhanovskaya, M.G., Vereshchagin, O.S., Bocharov, V.N., Shelukhina, Y.S., Lozhkin, M.S., Zaitsev, A.N., Nestola, F., 2022. Natural cubic perovskite, $Ca(Ti,Si,Cr)O_{3-\delta}$, a versatile potential host for rock-forming and less-common elements up to Earth's mantle pressure. American Mineralogist 107. 1936–1945. publisher: Mineralogical Society of America. https://doi.org/10.2138/am-2022-8186

Chen, B., Wang, W., Wu, Z., Wu, X., 2023. First-principles investigation on diffusion in stishovite and $CaCl_2$-type silica: implication for MORB viscosity in the lower mantle. Earth Planet. Sci. Lett. 615, 118198. https://doi.org/10.1016/j.epsl.2023.118198

Cottaar, S., Heister, T., Rose, I., Unterborn, C., 2014. Burnman: a lower mantle mineral physics toolkit. Geochem. Geophys. Geosyst. 15, 1164–1179. https://doi.org/10.1002/2013GC005122

Dobson, D., 2003. Oxygen Ionic Conduction in $MgSiO_3$ Perovskite. 139, 55–64. Elsevier BV. https://doi.org/10.1016/s0031-9201(03)00144-4

Dobson, D.P., Dohmen, R., Wiedenbeck, M., 2008. Self-diffusion of oxygen and silicon in $MgSiO_3$ perovskite. Earth Planet. Sci. Lett. 270, 125–129. https://doi.org/10.1016/j.epsl.2008.03.029

Domeier, M., Doubrovine, P.V., Torsvik, T.H., Spakman, W., Bull, A.L., 2016. Global correlation of lower mantle structure and past subduction. Geophys. Res. Lett. 43, 4945–4953. https://doi.org/10.1002/2016GL068827

Dou, P., Brodholt, J., Vočadlo, L., Ni, H., Li, Y., 2025. Ab initio evaluation of point defects in bridgmanite under lower mantle conditions. JGR Solid Earth 130. American Geophysical Union (AGU). https://doi.org/10.1029/2025JB031147

Dziewonski, A.M., Anderson, D.L., 1981. Preliminary reference Earth model. Phys. Earth Planet. Inter. 25, 297–356. https://doi.org/10.1016/0031-9201(81)90046-7

Evans, K., 2012. The redox budget of subduction zones. Earth Sci. Rev. 113, 11–32. https://doi.org/10.1016/j.earscirev.2012.03.003

Fei, H., Huang, R., Yang, X., 2017. $CaSiO_3$ perovskite may cause electrical conductivity jump in the topmost lower mantle. Geophys. Res. Lett. 44, https://doi.org/10.1002/2017GL075070

Figowy, S., Mohn, C.E., Caracas, R., 2024. Noble gas migration in silica polymorphs at Earth's mantle conditions. Earth Planet. Sci. Lett. 633, 118637. https://doi.org/10.1016/j.epsl.2024.118637

Glasser, L., 2012. Solid-State Energetics and Electrostatics: Madelung Constants and Madelung Energies, Inorg. Chem. 51, 2420–2424. American Chemical Society (ACS). https://doi.org/10.1021/ic2023852

Gréaux, S., Gautron, L., Andrault, D., Bolfan-Casanova, N., Guignot, N., Bouhifd, M.A., 2009. Experimental high pressure and high temperature study of the incorporation of uranium in Al-rich $CaSiO_3$ perovskite. Phys. Earth Planet. Inter. 174, 254–263. https://doi.org/10.1016/j.pepi.2008.06.010

Gu, T., Li, M., Mccammon, C., Lee, K.K.M., 2016. Redox-induced lower mantle density contrast and effect on mantle structure and primitive oxygen. Nat. Geosci. 9, 723–727. https://doi.org/10.1038/ngeo2772

Henkelman, G., Jónsson, H., 2000. Improved tangent estimate in the nudged elastic band method for finding minimum energy paths and saddle points. J. Chem. Phys. 113, 9978–9985. https://doi.org/10.1063/1.1323224

Henkelman, G., Uberuaga, B.P., Jónsson, H., 2000. A climbing image nudged elastic band method for finding saddle points and minimum energy paths. J. Chem. Phys. 113, 9901–9904. https://doi.org/10.1063/1.1329672

Hirel, P., 2015. Atomsk: a tool for manipulating and converting atomic data files. Comput. Phys. Commun. 197, 212–219. https://doi.org/10.1016/j.cpc.2015.07.012

Hirose, K., Takafuji, N., Sata, N., Ohishi, Y., 2005. Phase transition and density of subducted MORB crust in the lower mantle. Earth Planet. Sci. Lett. 237, 239–251. https://doi.org/10.1016/j.epsl.2005.06.035

Irifune, T., Ringwood, A., 1993. Phase transformations in subducted oceanic crust and buoyancy relationships at depths of 600–800 km in the mantle. Earth Planet. Sci. Lett. 117, 101–110. https://doi.org/10.1016/0012-821X(93)90120-X

Ishii, T., Kojitani, H., Akaogi, M., 2018. Phase relations and mineral chemistry in pyrolitic mantle at 1600–2200 °C under pressures up to the uppermost lower mantle: Phase transitions around the 660-km discontinuity and dynamics of upwelling hot plumes. Phys. Earth Planet. Inter. 274, 127–137. Elsevier BV. https://doi.org/10.1016/j.pepi.2017.10.005 .

Ishii, T., Miyajima, N., Criniti, G., Hu, Q., Glazyrin, K., Katsura, T., 2022. High pressure-temperature phase relations of basaltic crust up to mid-mantle conditions. Earth Planet. Sci. Lett. 584, 117472. https://doi.org/10.1016/j.epsl.2022.117472

Jain, A., Ong, S.P., Hautier, G., Chen, W., Richards, W.D., Dacek, S., Cholia, S., Gunter, D., Skinner, D., Ceder, G., Persson, K.A., 2013. Commentary: the materials project: a materials genome approach to accelerating materials innovation. APL Mater. 1, 11002. https://doi.org/10.1063/1.4812323

Karki, B.B., Khanduja, G., 2007. A computational study of ionic vacancies and diffusion in $MgSiO_3$ perovskite and post-perovskite. Earth Planet. Sci. Lett. 260, 201–211. https://doi.org/10.1016/j.epsl.2007.05.031

Klerk, N.J., van der Maas, E., Wagemaker, M., 2018. Analysis of Diffusion in Solid-State Electrolytes through MD Simulations, Improvement of the Li-Ion Conductivity in β-Li_3PS_4 as an Example. ACS Appl. Energy Mater. 1, 3230–3242. https://doi.org/10.1021/acsaem.8b00457

Kocer, E., Ko, T.W., Behler, J., 2022. Neural network potentials: a concise overview of methods. Annu. Rev. Phys. Chem. 73, 163–186. https://doi.org/10.1146/annurev-physchem-082720-034254

Kresse, G., Furthmüller, J., 1996. Efficiency of ab-initio total energy calculations for metals and semiconductors using a plane-wave basis set. Comput. Mater. Sci 6, 15–50. https://doi.org/10.1016/0927-0256(96)00008-0

Kresse, G., Joubert, D., 1999. From ultrasoft pseudopotentials to the projector augmented-wave method. Phys. Rev. B 59, 1758–1775. https://doi.org/10.1103/PhysRevB.59.1758

Li, W., Sunarso, J., Yang, Y., Chen, Y., Ge, C., Wang, W., Guo, Y., Ran, R., Zhou, W., 2024. Strategies for Improving Oxygen Ionic Conducting in Perovskite Oxides and their Practical Applications. Energy Reviews 3, 100085. Elsevier BV. https://doi.org/10.1016/j.enrev.2024.100085

Li, Z., Scandolo, S., 2022. Elasticity and viscosity of hcp iron at Earth's inner core conditions from machine learning-based large-scale atomistic simulations. Geophys. Res. Lett. 49, e2022GL101161. https://doi.org/10.1029/2022GL101161

Liu, Z., Ballaran, T.B., Huang, R., Frost, D.J., Katsura, T., 2019. Strong correlation of oxygen vacancies in bridgmanite with Mg/Si ratio. Earth and Planetary Science Letters 523, 115697. Elsevier BV. https://doi.org/10.1016/j.epsl.2019.06.037

Mehrer, H., 2007. Diffusion in Solids: Fundamentals, Methods, Materials, Diffusion-Controlled Processes. Number 155 in Springer series in solid state science. Springer, Berlin; New York.

Miyajima, N., Wang, L., Katsura, T., 2025. First observation of quenched davemaoite to ambient conditions: its electron diffraction pattern. Geophys. Res. Lett. 52, e2025GL115280. https://doi.org/10.1029/2025GL115280

Mohn, C.E., Caracas, R., Conrad, C.P., 2025. Lower mantle water distribution from ab initio proton diffusivity in bridgmanite. Earth and Planetary Science Letters 649, 119095. Elsevier BV. https://doi.org/10.1016/j.epsl.2024.119095

Myhill, R., Cottaar, S., Heister, T., Rose, I., Unterborn, C., Dannberg, J., Gassmoeller, R., 2023. Burnman - a python toolkit for planetary geophysics,geochemistry and thermodynamics. JOSS 8, 5389. https://doi.org/10.21105/joss.05389

Ono, S., Ito, E., Katsura, T., 2001. Mineralogy of subducted basaltic crust (MORB) from 25 to 37 GPa, and chemical heterogeneity of the lower mantle. Earth Planet. Sci. Lett. 190, 57–63. https://doi.org/10.1016/S0012-821X(01)00375-2

Peng, Y., Deng, J., 2023. Hydrogen diffusion in the lower mantle revealed by machine learning potentials. JGR Solid Earth 129, e2023JB028333. https://doi.org/10.1029/2023JB028333

Perdew, J.P., Burke, K., Ernzerhof, M., 1996. Generalized gradient approximation made simple. Phys. Rev. Lett 77, 3865–3868. https://doi.org/10.1103/PhysRevLett.77.3865

Poirier, J.P., 2000. Introduction to the Physics of the Earth's Interior. Cambridge University Press. 2nd ed. https://doi.org/10.1017/CBO9781139164467

Püthe, C., Kuvshinov, A., Khan, A., Olsen, N., 2015. A new model of Earth's radial conductivity structure derived from over 10 yr of satellite and observatory magnetic data. Geophys. J. Int. 203, 1864–1872. Oxford University Press (OUP). https://doi.org/10.1093/gji/ggv407

Robens, E., Rauschen, R., Kaub, J., Parras, J.P., Kemp, D., Freeman, C.L., Souza, R.A.D., 2022. Perovskite crystal symmetry and oxygen-ion transport: a molecular-dynamics study of perovskite. J. Mater. Chem. A 10, 2388–2397. https://doi.org/10.1039/D1TA06293J

Schie, M., Marchewka, A., Müller, T., Souza, R.A.D., Waser, R., 2012. Molecular dynamics simulations of oxygen vacancy diffusion in $SrTiO_3$. J. Phys. 24, 485002. https://doi.org/10.1088/0953-8984/24/48/485002

Singraber, A., Behler, J., Dellago, C., 2019a. Library-based LAMMPS implementation of high-dimensional neural network potentials. J. Chem. Theory Comput. 15, 1827–1840. https://doi.org/10.1021/acs.jctc.8b00770

Singraber, A., Morawietz, T., Behler, J., Dellago, C., 2019b. Parallel Multistream Training of High-Dimensional Neural Network Potentials. J. Chem. Theory Comput. 15, 3075–3092. American Chemical Society. https://doi.org/10.1021/acs.jctc.8b01092

Sinmyo, R., Pesce, G., Greenberg, E., Mccammon, C., Dubrovinsky, L., 2014. Lower mantle electrical conductivity based on measurements of Al,Fe-bearing perovskite under lower mantle conditions. Earth and Planetary Science Letters 393, 165–172. Elsevier BV. https://doi.org/10.1016/j.epsl.2014.02.049

Souza, R.A., 2015. Oxygen diffusion in $SrTiO_3$ and related perovskite oxides. Adv. Funct. Mater. 25, 6326–6342. https://doi.org/10.1002/adfm.201500827

Stixrude, L., Lithgow-Bertelloni, C., 2011. Thermodynamics of mantle minerals - II. phase equilibria. Geophys. J. Int. 184, 1180–1213. https://doi.org/10.1111/j.1365-246X.2010.04890.x

Sun, W., Tao, R., Zhu, J., Wang, C., Ishii, T., Li, Y., 2024. K- and Na-rich davemaoite inclusion in diamond is not inherited from deeply subducted oceanic crusts. Earth Planet. Sci. Lett. 637, 118741. https://doi.org/10.1016/j.epsl.2024.118741

Thompson, A.P., Aktulga, H.M., Berger, R., Bolintineanu, D.S., Brown, W.M., Crozier, P.S., In'T VeldP.J., Kohlmeyer, A., Moore, S.G., Nguyen, T.D., Shan, R., Stevens, M.J., Tranchida, J., Trott, C., Plimpton, S.J., 2022. LAMMPS - a flexible simulation tool for particle-based materials modeling at the atomic, meso, and continuum scales. Comput. Phys. Commun. 271, 108171. https://doi.org/10.1016/j.cpc.2021.108171

Tokita, A.M., Behler, J., 2023. How to train a neural network potential. J. Chem. Phys. 159, 121501. https://doi.org/10.1063/5.0160326

Verhoeven, O., Thébault, E., Saturnino, D., Houliez, A., Langlais, B., 2021. Electrical conductivity and temperature of the Earth's mantle inferred from Bayesian inversion of Swarm vector magnetic data. Physics of the Earth and Planetary Interiors 314, 106702. Elsevier BV. https://doi.org/10.1016/j.pepi.2021.106702

Vineyard, G.H., 1957. Frequency factors and isotope effects in solid state rate processes. J. Phys. Chem. Solids 3, 121–127. https://doi.org/10.1016/0022-3697(57)90059-8

Virtanen, P., Gommers, R., Oliphant, T.E., Haberland, M., Reddy, T., Cournapeau, D., Burovski, E., Peterson, P., Weckesser, W., Bright, J., Walt, S.J.V.D., Brett, M., Wilson, J., Millman, K.J., Mayorov, N., Nelson, A.R.J., Jones, E., Kern, R., Larson, E., Carey, C.J., Polat, I., Feng, Y., Moore, E.W., Vanderplas, J., Laxalde, D., Perktold, J., Cimrman, R., Henriksen, I., Quintero, E.A., Harris, C.R., Archibald, A.M., Ribeiro, A.H., Pedregosa, F., Mulbregt, P.V., Vijaykumar, A., Bardelli, A.P., Rothberg, A., Hilboll, A., Kloeckner, A., Scopatz, A., Lee, A., Rokem, A., Woods, C.N., Fulton, C., Masson, C., Häggström, C., Fitzgerald, C., Nicholson, D.A., Hagen, D.R., Pasechnik, D.V., Olivetti, E., Martin, E., Wieser, E., Silva, F., Lenders, F., Wilhelm, F., Young, G., Price, G.A., Ingold, G.L., Allen, G.E., Lee, G.R., Audren, H., Probst, I., Dietrich, J.P., Silterra, J., Webber, J.T., Slavič, J., Nothman, J., Buchner, J., Kulick, J., Schönberger, J., Cardoso, J.L.D.M., Reimer, J.V., Harrington, J., Rodríguez, J., Nunez-Iglesias, J.L.C., Kuczynski, J., Tritz, J., Thoma, K., Newville, M., Kümmerer, M., Bolingbroke, M., Tartre, M., Pak, M., Smith, M., Nowaczyk, N.J., Shebanov, N., Pavlyk, N., Brodtkorb, O., Lee, P.A., Mcgibbon, P., Feldbauer, R.T., Lewis, R., Tygier, S., Sievert, S., Vigna, S., Peterson, S., More, S., Pudlik, S., Oshima, T., Pingel, T. J., Robitaille, T.P., Spura, T., Jones, T.R., Cera, T., Leslie, T., Zito, T., Krauss, T., Upadhyay, U., Halchenko, Y.O., Vázquez-Baeza, Y., 2020. SciPy 1.0: fundamental algorithms for scientific computing in Python. Nat. Methods 17, 261–272. . https://doi.org/10.1038/s41592-019-0686-2

Wang, L., Miyajima, N., Wang, F., Katsura, T., 2025a. Persistence of davemaoite at lower-mantle conditions. Nat. Geosci. 18, 365–369. https://doi.org/10.1038/s41561-025-01657-9

Wang, Z., He, Y., Mao, H.K., Kim, D.Y., 2025b. Superionicity of oxygen-deficient davemaoite and its impact on the deep-Earth oxidation cycle. Sci. Adv. 11, eadu8401. https://doi.org/10.1126/sciadv.adu8401

White, R.S., Mckenzie, D., O'nions, R.K., 1992. Oceanic crustal thickness from seismic measurements and rare earth element inversions. J. Geophys. Res. 97, 19683–19715 American Geophysical Union (AGU). https://doi.org/10.1029/92JB01749

Xu, F., Yamazaki, D., Sakamoto, N., Sun, W., Fei, H., Yurimoto, H., 2017. Silicon and oxygen self-diffusion in stishovite: implications for stability of SiO_2-rich seismic reflectors in the mid-mantle. Earth Planet. Sci. Lett. 459, 332–339. https://doi.org/10.1016/j.epsl.2016.11.044

Xu, J., Yamazaki, D., Katsura, T., Wu, X., Remmert, P., Yurimoto, H., Chakraborty, S., 2011. Silicon and magnesium diffusion in a single crystal of $MgSiO_3$ perovskite. J. Geophys. Res.. 116, B12205. https://doi.org/10.1029/2011JB008444

Xu, Y., Mccammon, C., 2002. Evidence for ionic conductivity in lower mantle $(Mg,Fe)(Si,Al)O_3$ perovskite. J. Geophys. Res.. 107. American Geophysical Union (AGU). https://doi.org/10.1029/2001JB000677

Yao, H., Ren, Z., Pan, K., Tang, J., Zhang, K., 2023. A global mantle conductivity model derived from 8 years of swarm satellite magnetic data. Earth Planet. Phys. 7, 49–56. https://doi.org/10.26464/epp2023011

Yashima, M., 2008. Crystal structures, structural disorders and diffusion paths of ionic conductors from diffraction experiments. Solid State Ionics. 179, 797–803. Elsevier BV. https://doi.org/10.1016/j.ssi.2007.12.099

Yoshino, T., Kamada, S., Zhao, C., Ohtani, E., Hirao, N., 2016. Electrical conductivity model of Al-bearing bridgmanite with implications for the electrical structure of the Earth's lower mantle. Earth Planet. Sci. Lett. 434, 208–219. https://doi.org/10.1016/j.epsl.2015.11.032